Nano Research

ISSN 1998-0124 CN 11-5974/O4
https://doi.org/10.1007/s12274-021-3332-0

Research Article

High elasticity of $CsPbBr_3$ perovskite nanowires for flexible electronics

Xiaocui Li[1,§], You Meng[2,§], Rong Fan[1,3,§], Sufeng Fan[1], Chaoqun Dang[1], Xiaobin Feng[1], Johnny C. Ho[2] (✉), and Yang Lu[1,4] (✉)

Nano Res., **Just Accepted Manuscript • https://doi.org/10.1007/s12274-021-3332-0**
http://www.thenanoresearch.com on Jan. 15, 2021

Just Accepted

Address correspondence to First A. Firstauthor, email1; Third C. Thirdauthor, email2

TABLE OF CONTENTS (TOC)

High elasticity of $CsPbBr_3$ perovskite nanowires for flexible electronics

Xiaocui Li[1], You Meng[2], Rong Fan[1,3], Sufeng Fan[1], Chaoqun Dang[1], Xiaobin Feng[1], Johnny C. Ho[2,*], Yang Lu[1,4,*]

1 City University of Hong Kong, China
2 City University of Hong Kong, China
3 Dalian University of Technology, China
4 Shenzhen Research Institute of City University of Hong Kong, China

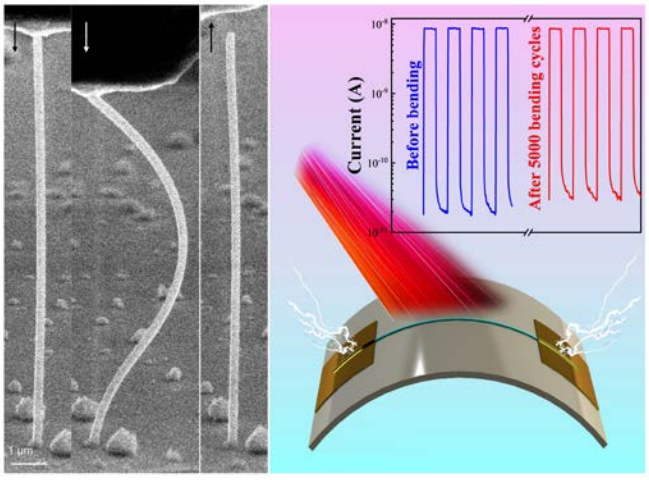

High flexural elasticity (~4% to ~5.1%) has been achieved in $CsPbBr_3$ nanowires. The flexible photodetectors fabricated by $CsPbBr_3$ nanowires exhibited excellent mechanical reliability during 5000 times bending tests.

Johnny C. Ho, https://www.cityu.edu.hk/mse/staff.aspx#~HO-johnny
Yang Lu, http://www.cityu.edu.hk/mne/yanglu/

Nano Research
DOI (automatically inserted by the publisher)
Research Article
ISSN 1998-0124
CN 11-5974/O4

High elasticity of $CsPbBr_3$ perovskite nanowires for flexible electronics

Xiaocui Li[1,§], You Meng[2,§], Rong Fan[1,3,§], Sufeng Fan[1], Chaoqun Dang[1], Xiaobin Feng[1], Johnny C. Ho[2] (✉), Yang Lu[1,4] (✉)

[1] *Department of Mechanical Engineering, City University of Hong Kong, Hong Kong SAR 999077, China*
[2] *Department of Materials Science and Engineering, City University of Hong Kong, Hong Kong SAR 999077, China*
[3] *School of Automotive Engineering, Dalian University of Technology, Dalian 116024, China*
[4] *Nano-Manufacturing Laboratory (NML), Shenzhen Research Institute of City University of Hong Kong, Shenzhen 518057, China*
[§] *These authors contribute equally*

Received: 19 October 2020
Revised: 5 January 2021
Accepted: 11 January 2021

KEYWORDS
Perovskite nanowire, $CsPbBr_3$, nanomechanics, in situ testing, elasticity, flexible electronics

ABSTRACT

Due to the enhanced ambient structural stability and excellent optoelectronic properties, all-inorganic metal halide perovskite nanowires have become one of the most attractive candidates for flexible electronics, photovoltaics and optoelectronics. Their elastic property and mechanical robustness become the key factors for device applications under realistic service conditions with various mechanical loadings. Here, we demonstrate that high tensile elastic strain (~4% to ~5.1%) can be achieved in vapor-liquid-solid-grown single-crystalline $CsPbBr_3$ nanowires through in situ scanning electron microscope (SEM) buckling experiments. Such high flexural elasticity can be attributed to the structural defect-scarce, smooth surface, single-crystallinity and nanomechanical size effect of $CsPbBr_3$ nanowires. The mechanical reliability of $CsPbBr_3$ nanowire-based flexible photodetectors was examined by cyclic bending tests, with no noticeable performance deterioration observed after 5000 cycles. The above results suggest great application potential for using all-inorganic perovskite nanowires in flexible electronics and energy harvesting systems.

1 Introduction

In recent years, perovskite materials have shown tremendous potential in developing photovoltaic devices, light-emitting devices and displays because of their excellent light-harvesting capability, high charge carrier mobility, long carrier diffusion length, high color purity and wide color gamut [1-3], etc. Among them, all-inorganic metal halide perovskites are attracting more and more attention due to their

Address correspondence to Johnny C. Ho, johnnyho@cityu.edu.hk; Yang Lu, yanglu@cityu.edu.hk

enhanced ambient stability than hybrid perovskites and retained superior optoelectronic properties [4-6]. As a promising candidate in the field of flexible electronics (e.g. flexible solar cells, artificial skins, wearable electronic textiles) [7-9], perovskite materials are expected to function under different mechanical strain states for practical applications. Therefore, it's crucial for perovskites to achieve high mechanical elasticity. Decreasing the sample size to micro/nanoscale has been proved to be a feasible way to obtain substantial elasticity in crystalline materials that are brittle at the bulk scale [10-19]. Notably, elastic strain as high as ~16% has been achieved in Si nanowire through uniaxial *in situ* tensile straining in a SEM [16]. Maximum tensile strains up to ~9-13% have been reported by bending diamond nanoneedles inside SEM or transmission electron microscope (TEM) [18, 19]. Besides, nanostructured semiconductors showed much better performances in developing electronics than their bulk or thin-film counterparts for enhanced carrier mobilities [20-22]. The above researches give valuable insights for developing next-generation flexible electronics by resorting to all-inorganic perovskite nanowires.

Furthermore, as perovskites serve as the most crucial and believed to be the mechanically weakest component among flexible devices, their elastic limit determines the flexibility and reliability of devices. However, at present, the flexibility of perovskite materials was usually revealed by the bending tests of whole electronics [7, 23, 24], in which the device performance commonly degraded with increasing bending cycles and degree [7, 25, 26]. Whereas only limited attention has been paid to explore the underlying mechanisms of performance deterioration by investigating the deformation and microstructure evolution in free-standing perovskite materials [27]. Experimentally probing the intrinsic mechanical properties (particularly, the elastic limit) and structural evolution of individual perovskite nanostructures through nanomechanical approach is essential for guiding the future devices design and reliable applications.

Here, in this study, we report the high flexural elasticity of "individual" all-inorganic $CsPbBr_3$ perovskite nanowires (NWs) through the *in situ* SEM compression-induced buckling experiments, with the finite element method (FEM) simulations were complemented to quantify the local strain distributions of deformed NWs [19]. Furthermore, we demonstrate the excellent mechanical reliability of $CsPbBr_3$ NW-based flexible photodetectors (PDs) through cyclic bending tests. The present results evidently indicate the potential of $CsPbBr_3$ NWs for high-performance flexible electronics.

2 Experimental

2.1 Material Synthesis

The materials used in this study are all-inorganic perovskite $CsPbBr_3$ nanowires prepared by direct Vapor-Liquid-Solid synthesis method. All chemicals used in this work were purchased from Sigma-Aldrich. First of all, an aqueous suspension containing 150-nm-diameter Sn nanoparticles (≥99 %, Aldrich) was drop-casted onto the 50 nm thick thermally grown SiO_2/Si substrates, as the growth substrate. To prepare the $CsPbBr_3$ source powder, CsBr and $PbBr_2$ powers with a molar ratio of 2:1 were mixed together and then annealed at 430 °C for 30 min. In a CVD systhesis system, the $CsPbBr_3$ source powder and growth substrates were placed at the high-temperature zone (440 °C) and low-temperature zone (310 °C), respectively. During the growth, the chamber pressure was set to 1.2 Torr, whereas the Ar gas with a flow speed of 80 sccm was used as a carrier gas. After the growth duration, $CsPbBr_3$ NWs were obtained on the growth substrates.

2.2 Material Characterization

The TEM characterization of nanowires were obtained by using a field-emission transmission electron microscope (JEOL, JEM-2100F FE-TEM). The SEM images were obtained by using a field-emission scanning electron microscope (FEI, Quanta 450 FE-SEM). X-ray diffraction (XRD) test was conducted on a Philips powder diffractometer. Elemental mapping was performed on an energy-dispersive X-ray spectroscopy (EDS) detector attached to the FEI Quanta 450 FE-SEM.

2.3 *in situ* Nanomechanical characterization

The protocol of *in situ* compressive mechanical test of $CsPbBr_3$ NWs was based on a quantitative nanoindenter (Hysitron PI85 PicoIndenter) in conjunction with a SEM (FEI Quanta 450 field-emission SEM). A substrate with $CsPbBr_3$ nanowires grown vertically on it has been fixed on the stage, then careful adjustment of the relative position of indenter and NW was conducted to ensure they are well-contacted. The uniaxial compressive tests can be achieved by the downwards movements of diamond indenter under displacement control mode with a constant loading velocity of 20 nm/s (when the desired loading displacement amplitude exceeded the displacement range of nanoindenter, sample stage was firstly raised upwards to achieve large relative displacement). The deformation process of NW was simultaneously recorded by SEM.

2.4 FEM analyses

We carried out the finite element method (FEM) simulation using the commercial ABAQUS software package (Dassault Systèmes Simulia Corp.) to quantify the strain distribution of deformed $CsPbBr_3$ NWs under buckling/bending [19]. Nonlinear elastic deformation was taken into account in this study. The Young's modulus (E) is 20 GPa and the Poisson ratio (υ) is 0.3. In this simulation, the displacement and rotation at the bottom of the NW was fixed; the displacement constraint was applied to the top of the NW. For the NW in Figure 2, according to the calculation of the length of NW before and after deformation, it can be seen that the deformation of NW is out of the observing plane. The strain state was obtained by following the actual rotated geometry for the NW. Since the difference between the maximum principal strain and maximum tensile strain within the NW surface is actually less than 0.5% in FEM simulations, the extracted maximum principal strain from FEM simulations for each NW is equivalent to the maximum elastic tensile strain.

2.5 Device fabrication and characterization

To fabricate $CsPbBr_3$ NW-based photodetectors, a contact transfer method was used to transfer the $CsPbBr_3$ NWs from the growth substrates to the polyimide (PI) substrates. After that, shadow mask was employed to define the source and drain regions (channel lengths are 10 μm), and then 50-nm-thick Au electrodes were deposited by thermal evaporation. Agilent 4155C semiconductor analyzer was used to examine the electrical performance of $CsPbBr_3$ NW devices in a standard probe station. For photodetector measurements, the wavelength of light source was 450 nm, and the incident light power was measured by a power meter (PM400, Thorlabs).

3 Results and discussion

Fig. 1(a) shows the bright-field transmission electron microscope (TEM) image of a typical $CsPbBr_3$ NW with a diameter of ~130 nm. The inset depicts the selected-area electron diffraction (SAED) pattern of the NW, which is taken along [100] zone axis, illustrating the single-crystalline cubic structure and <100>-oriented growth direction of the NW. The crystal structure was also verified by the XRD (Figure S1 in the Electronic Supplementary Material (ESM)), in which only diffraction peaks of cubic $CsPbBr_3$ were detected. The high resolution TEM (HRTEM) in Fig. 1(b) illustrates the excellent crystallinity and defect-scarce characteristic of the VLS-grown $CsPbBr_3$ NW. Figs. 1(c)-(f) are the SEM image and corresponding EDS mappings of another $CsPbBr_3$ NW, showing the uniform distribution of Cs, Pb and Br elements. From above, the $CsPbBr_3$ NWs possess a quite good crystal quality with smooth surface, uniform diameter and defect-scarce single-crystallinity, these features are significant for material's mechanical properties to avoid premature failure. The configuration of *in situ* compression experiments was depicted in Figs. 1(g) and (h), in brief, a flat diamond indenter (Fig. 1(g)) was used to impose mechanical load on $CsPbBr_3$ NWs that

grown vertically on the substrate (Fig. 1(h)) and introduce bending/buckling to the NW samples.

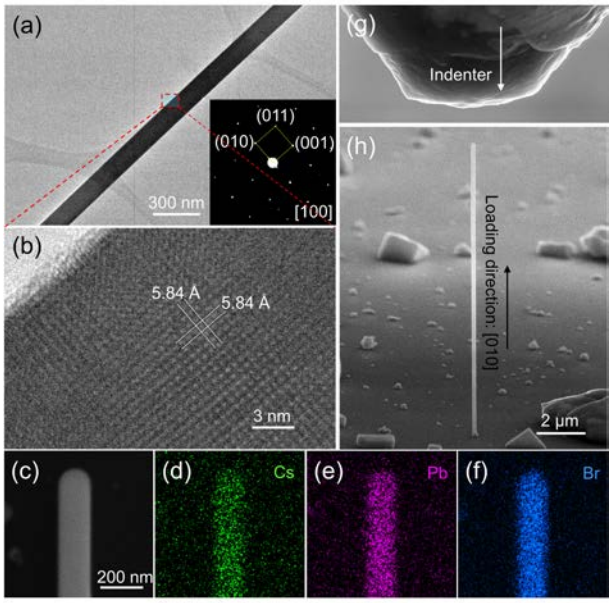

Figure 1 Material characterization and experimental configuration. (a) Bright-field transmission electron microscope (TEM) image of a typical $CsPbBr_3$ nanowire (NW). Inset shows the corresponding selected-area electron diffraction (SAED) pattern; (b) High-resolution TEM (HRTEM) image of the region marked in (a); (c-f) Scanning electron microscope (SEM) image of another $CsPbBr_3$ NW and corresponding energy-dispersive X-ray spectroscopy (EDS) mappings of Cs, Pb and Br elements, respectively; (g, h) SEM images of the diamond indenter and a nanowire that grown vertically on the substrate, respectively.

It is well-acknowledged that loading-unloading is the most unambiguous method for assessing the elasticity and plasticity of deformation. For elastic deformation, the deformed material could fully recover its original shape when it is unloaded; otherwise, plastic deformation occurred. Therefore, to better discern whether the deformation mode of $CsPbBr_3$ NWs is plastic or elastic, multiple loading-unloading tests were conducted. Figure 2 shows the process of *in situ* loading-unloading buckling deformation of a representative $CsPbBr_3$ NW that extracted from Supplementary Movie 1. The NW has a diameter of ~215 nm and a length of ~14.5 μm (i.e. aspect ratio of ~67). Soon after loading, the NW buckled into a loop (Fig. 2(b)). Figs. 2(c) and (d) illustrate the increasing loop curvature under the gradually increased displacement. When the NW was unloaded (Fig. 2(e)), surprisingly, it totally recovered to its original shape, which is a strong evidence for the fully reversible elastic deformability of the $CsPbBr_3$ NW.

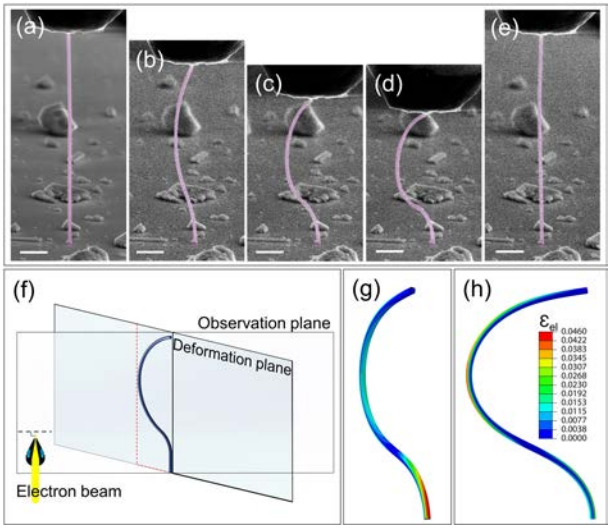

Figure 2 Elastic buckling of a typical $CsPbBr_3$ NW. (a-e) Loading-unloading process by *in situ* nanomechanical compression; (f) Spatial relationship of the observation plane which is vertical to electron beam and the NW deformation plane; Finite element method (FEM) simulations showing the elastic tensile strain distribution of the NW geometry prior to unloading in (d) on: (g) observation plane, (h) deformation plane, respectively. Scale bar in all the figures: 2 μm.

FEM simulations were complemented for the strain distribution of the deformed NW. Based on the original NW dimension and its geometry during deformation, it is found that the deformation plane of NW was not parallel with the observation plane which is perpendicular to the electron beam incident direction (Fig. 2(f)). The FEM simulations in Figs. 2(g) and (h) fully reproduced the NW geometry in Fig. 2(d) (on observation plane) and its' actual geometry on deformation plane, respectively. A maximum local tensile strain of ~4.6% was inferred. This high elasticity is especially striking for perovskite materials, which are commonly

regarded as fragile. The NW also exhibited considerable plastic deformability in the following loading-unloading cycles, as illustrated in Figure S2 in the ESM and Supplementary Movie 2.

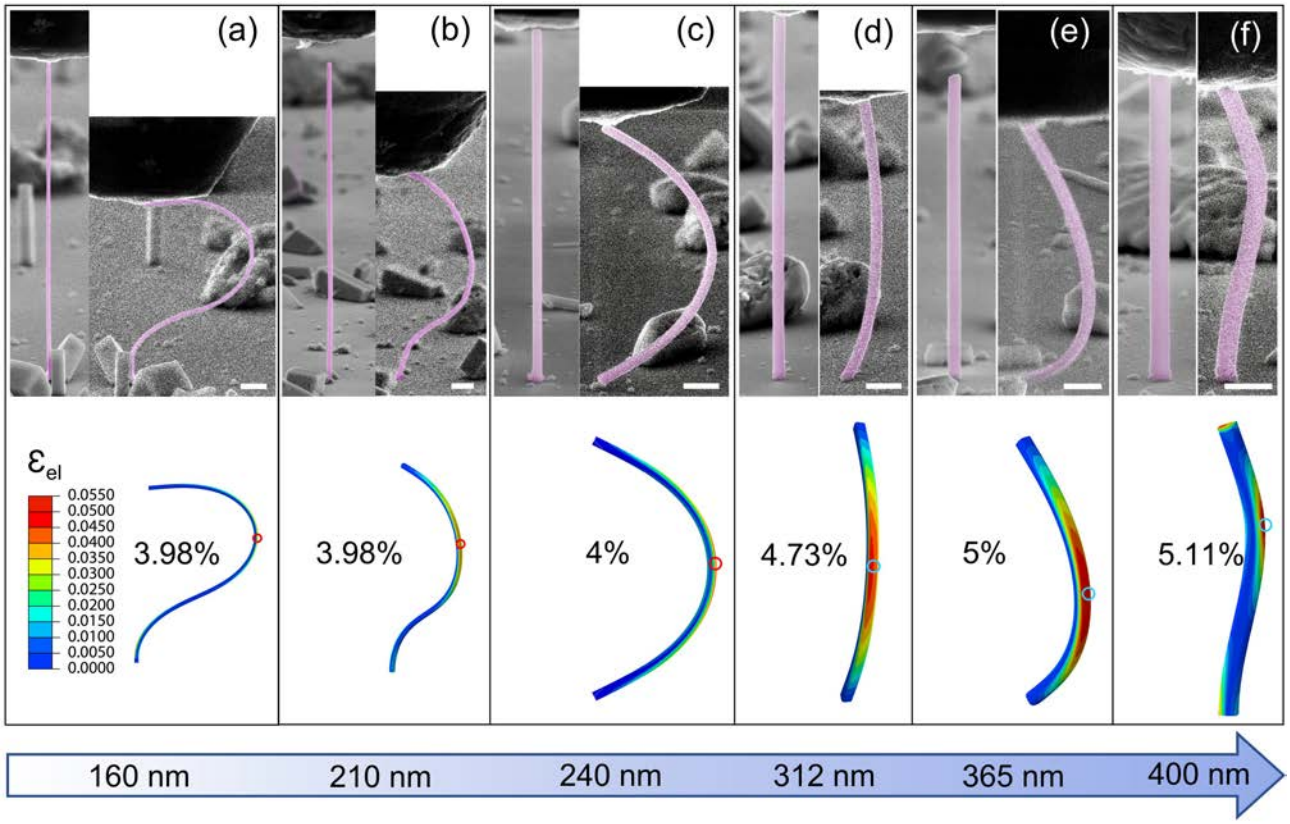

Figure 3 Size-effect on the elasticity of $CsPbBr_3$ NWs. (a-f) SEM images of the original geometry and the maximum elastic deformation of each NW, the FEM strain distribution of NWs at the largest elastic deformation were accompanied below. Scale bar in all the figures: 1 μm.

As the NWs prepared by VLS method are not uniform in size, to check the potential size effect on mechanical property and reproducibility of high elasticity in $CsPbBr_3$ NWs, a series of *in situ* compressions of nanowires with diameter ranging from 160 nm to 400 nm were conducted. Figure 3 shows the original geometry and the maximum elastic deformation of each NW. The FEM strain distribution on NWs at the largest elastic deformation were accompanied below each NW. All the NWs exhibited remarkable elastic deformability. For the NWs with diameter of 160 nm, 210 nm and 240 nm, a maximum flexural elastic strain of ~4% can be obtained. While for the NWs with larger diameter, the maximum flexural elastic strain increased with diameter. Through Figs. 3(d)-(f), the maximum strains were ~4.73%, ~5%, ~5.11% for NWs with diameter of 312 nm, 365 nm and 400 nm, respectively. This size-related elasticity can be qualitatively deduced from the equation of bending strain: $\varepsilon=r/(r+R)\%$, where r and R are the radius of NW and the radius of flexural curvature of deformed NW [14]. The maximum local strain of a specific NW is obtained at the minimum radius of curvature. As the NW diameter increases, the NW diameter grows faster than the flexural curvature, thus leading to a higher strain.

The excellent elasticity of $CsPbBr_3$ NWs mainly comes from two aspects: Firstly, the elasticity of crystalline nanomaterials generally superior to their bulk counterparts. As the materials' characteristic dimensions are reduced to the nanoscale, the

internal defects are extremely eliminated. Thus, the probability for starting a surface Griffith crack or inner grain nanocrack is linearly reduced. Secondly, the catalytic VLS growth method used in this study enables the NWs to achieve pristine single crystallinity, defect-scarce interior structure, smooth surface and uniform diameter, which are essential for NWs to avoid the stress localization, to withstand a larger range of deformation without premature fracture. It's worth mentioning that, although catalytic VLS growth method is well-known for ease of harvesting high-quality nanostructures [28, 29], non-catalytic vapor-solid (VS) growth method was more prevalence for lead halide perovskites due to the difficulty to handle ternary material systems through VLS synthesis method. The success in applying VLS method to fabricate high-quality $CsPbBr_3$ NWs [30] will give inspirations to the synthesis of other perovskite nanostructures.

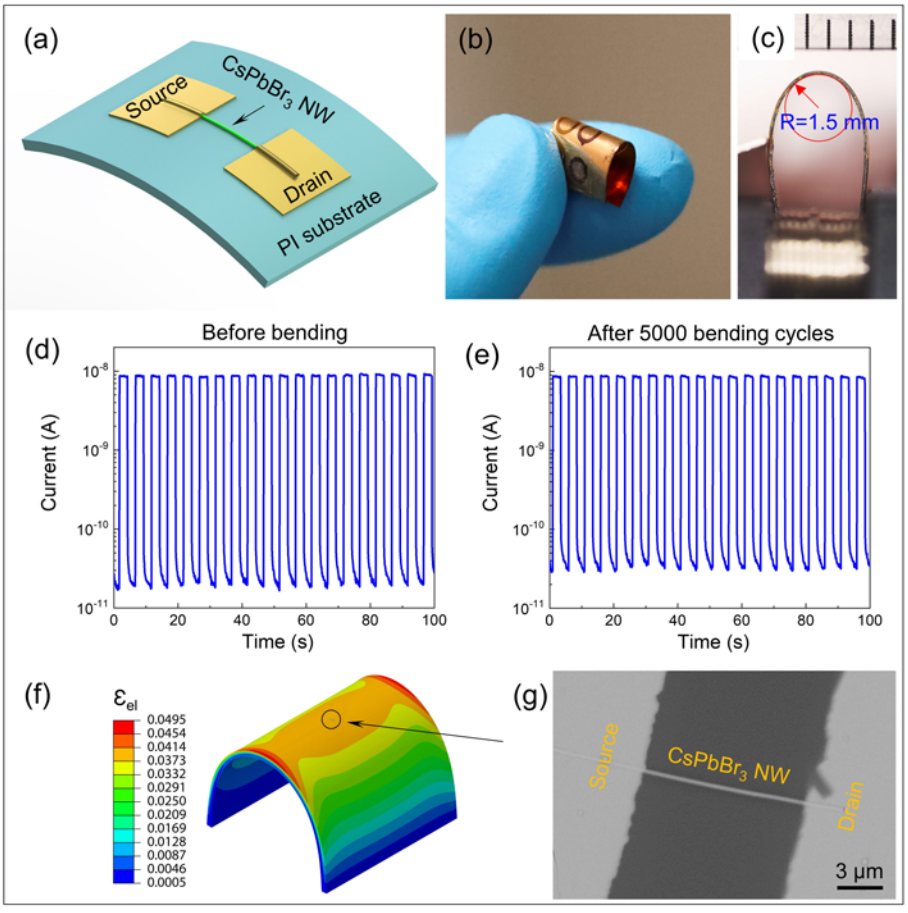

Figure 4 Mechanical reliability of $CsPbBr_3$ NW-based photodetectors (PDs) through bending tests. (a) Architecture of a flexible PD device; (b) Optical image of a PD device showing excellent flexibility; (c) Side view of the PD device under bending status. The bending radius is 1.5 mm with a real ruler illustrated on the top as scale bar; (d, e) The device photocurrent under on/off switching light illumination (0.2 Hz) as a function of time that measured before bending tests and after 5000 bending cycles, respectively; (f) FEM simulation of the PD device at a bending radius of 1.5 mm, reproducing the shape in (c), the location of Au electrodes and NW indicated by the circle; (g) SEM image of the PD, showing the NW was well-bonded on substrate by Au electrodes

Lastly, the $CsPbBr_3$ NWs were packaged into flexible photodetectors (PDs) to verify the cyclic mechanical performance for flexible device applications. Fig. 4(a) gives an architecture of flexible PD, in which the Au source and drain electrodes were connected by a $CsPbBr_3$ NW

channel. Flexible polyimide (PI) substrate was employed such that PD could achieve large bending deformation, as illustrated by Fig. 4(b). The performance of the as-fabricated PD was characterized in Figure S3 of ESM. A total of 5000 bending cycles were performed on a PD at a fixed bending radius of 1.5 mm at ambient environment, as shown in Fig. 4(c), in which a real ruler was placed on the top as a scale bar. The device photocurrent under on/off switching light illumination was evaluated before and after 5000 bending cycles, as depicted in Figs. 4(d) and (e), respectively (photocurrent after 1000, 2000 and 3000 bending cycles were shown in Figure S4 of ESM). These photocurrent measurements suggest there is no noticeable photocurrent deterioration after bending tests.

Such robust device performance in bending tests can be attributed to the superior flexural elasticity of $CsPbBr_3$ NWs. As shown in the FEM simulation of PD device when it was bent at a radius of 1.5 mm (Fig. 4(f)), the strain on the middle of the substrate where the NW was located is around ~3.9%. Supposing the NW was perfectly bonded on the substrate by the Au electrodes, the maximum tensile strain on it will be same with the substrate where it was bonded. The SEM image of PD in Fig. 4(g) suggests a satisfactory bonding condition of the NW. Thus, the strain on it is ≤3.9%. Since the value is below the elastic limits that achieved in free-standing NWs (~4% to ~5.11%, as demonstrated in Figures 2 and 3), the NW-based PD is totally "safe" under present bending deformation; the structural damage, e.g. plastic deformation, crack initiation, and concurrent deterioration of photoelectric performance can be avoided. As the strain on substrate surface can be lowered by decreasing the substrate thickness [31], one can expect to apply $CsPbBr_3$ NWs on ultra-thin flexible substrates to serve at more severe deformation conditions. Besides, the PD reliability also benefited from the good structural stability (*i.e.* resistance to humidity and oxygen) of the all-inorganic NWs at ambient environment. The environmental stability of PD was checked, with 90% of initial photocurrent can be retained after 12 hours exposure at ambient conditions, as shown in Figure S5 of ESM. The long-term stability of $CsPbBr_3$ NW device can be further enhanced through surface passivation with MoO_3 shells, as reported in our recent work [5]. The present work has profound significance for their practical applications.

4. Conclusion

In summary, we uncovered the excellent flexural elasticity of VLS-grown $CsPbBr_3$ NWs through *in situ* nanomechanical measurements, where the maximum local tensile elasticity as high as ~4% to ~5.11% can be achieved. The application of $CsPbBr_3$ NWs in developing flexible devices was then revealed by cyclic bending tests of the NW photodetectors, of which the performance was almost unchanged after 5000 bending cycles. With the merits shown above, the VLS-grown $CsPbBr_3$ NWs were proven to be one of the most promising candidates for flexible optoelectronic devices that are even capable to function under extreme deformation conditions. Experimentally achieving such high elasticity in $CsPbBr_3$ NWs is also significant for their potential applications in "elastic strain engineering (ESE)", which could potentially change their physical and chemical properties through mechanical straining alone [32, 33].

Acknowledgements

This work was supported by Hong Kong Research Grant Council (RGC) (Grant No. CityU 11207416 and CityU 11306520), City University of Hong Kong (Grant No. 9667194), and National Natural Science Foundation of China under Grant No. 11922215.

Electronic Supplementary Material: Supplementary material (XRD of $CsPbBr_3$ NWs, plastic deformation and fracture of $CsPbBr_3$ NW, performance characterization of as-fabricated $CsPbBr_3$ NW-based PD, PD performance after 1000, 2000 and 3000

bending cycles, environmental stability of PD, Supplementary Movies 1 and 2) is available in the online version of this article at http://dx.doi.org/10.1007/s12274-***-****-* (automatically inserted by the publisher).

References

[1] Stranks, S. D.; Eperon, G. E.; Grancini, G.; Menelaou, C.; Alcocer, M. J.; Leijtens, T.; Herz, L. M.; Petrozza, A.; Snaith, H. J. Electron-hole diffusion lengths exceeding 1 micrometer in an organometal trihalide perovskite absorber. *Science* **2013,** *342*, 341-344.

[2] Baikie, T.; Fang, Y. N.; Kadro, J. M.; Schreyer, M.; Wei, F. X.; Mhaisalkar, S. G.; Graetzel, M.; White, T. J. Synthesis and crystal chemistry of the hybrid perovskite $(CH_3NH_3)PbI_3$ for solid-state sensitised solar cell applications. *J. Mater. Chem. A* **2013,** *1*, 5628-5641.

[3] Lu, M.; Zhang, Y.; Wang, S. X.; Guo, J.; Yu, W. W.; Rogach, A. L. Metal halide perovskite light -emitting devices: Promising technology for next -generation displays. *Adv. Funct. Mater.* **2019,** *29*, 1902008.

[4] Saliba, M.; Matsui, T.; Seo, J. Y.; Domanski, K.; Correa-Baena, J. P.; Nazeeruddin, M. K.; Zakeeruddin, S. M.; Tress, W.; Abate, A.; Hagfeldt, A. Cesium-containing triple cation perovskite solar cells: Improved stability, reproducibility and high efficiency. *Energy Environ. Sci.* **2016,** *9*, 1989-1997.

[5] Meng, Y.; Lai, Z. X.; Li, F. Z.; Wang, W.; Yip, S. P.; Quan, Q.; Bu, X. M.; Wang, F.; Bao, Y.; Hosomi, T. et al. Perovskite core-shell nanowire transistors: Interfacial transfer doping and surface passivation. *ACS Nano* **2020**.

[6] Sutton, R. J.; Eperon, G. E.; Miranda, L.; Parrott, E. S.; Kamino, B. A.; Patel, J. B.; Hörantner, M. T.; Johnston, M. B.; Haghighirad, A. A.; Moore, D. T. et al. Bandgap-tunable cesium lead halide perovskites with high thermal stability for efficient solar cells. *Adv. Energy Mater.* **2016,** *6*, 1502458.

[7] Li, Y. W.; Meng, L.; Yang, Y. M.; Xu, G. Y.; Hong, Z. R.; Chen, Q.; You, J. B.; Li, G.; Yang, Y.; Li, Y. F. High-efficiency robust perovskite solar cells on ultrathin flexible substrates. *Nat. Commun.* **2016,** *7*, 1-10.

[8] Khang, D. Y.; Jiang, H. Q.; Huang, Y.; Rogers, J. A. A stretchable form of single-crystal silicon for high-performance electronics on rubber substrates. *Science* **2006,** *311*, 208-212.

[9] Liu, Z.; Xu, J.; Chen, D.; Shen, G. Z. Flexible electronics based on inorganic nanowires. *Chem. Soc. Rev.* **2015,** *44*, 161-92.

[10] Hoffmann, S.; Utke, I.; Moser, B.; Michler, J.; Christiansen, S. H.; Schmidt, V.; Senz, S.; Werner, P.; Gösele, U.; Ballif, C. Measurement of the bending strength of vapor-liquid-solid grown silicon nanowires. *Nano Lett.* **2006,** *6*, 622-625.

[11] Hsin, C. L.; Mai, W. J.; Gu, Y. D.; Gao, Y. F.; Huang, C. T.; Liu, Y. Z.; Chen, L. J.; Wang, Z. L. Elastic properties and buckling of silicon nanowires. *Adv. Mater.* **2008,** *20*, 3919-3923.

[12] Zhu, Y.; Xu, F.; Qin, Q. Q.; Fung, W. Y.; Lu, W. Mechanical properties of vapor-liquid-solid synthesized silicon nanowires. *Nano Lett.* **2009,** *9*, 3934-3939.

[13] Wang, L. H.; Zheng, K.; Zhang, Z.; Han, X. D. Direct atomic-scale imaging about the mechanisms of ultralarge bent straining in Si nanowires. *Nano Lett.* **2011,** *11*, 2382-2385.

[14] Zheng, K.; Han, X. D.; Wang, L. H.; Zhang, Y. F.; Yue, Y. H.; Qin, Y.; Zhang, X. N.; Zhang, Z. Atomic mechanisms governing the elastic limit and the incipient plasticity of bending Si nanowires. *Nano Lett.* **2009,** *9*, 2471-2476.

[15] Stan, G.; Krylyuk, S.; Davydov, A. V.; Levin, I.; Cook, R. F. Ultimate bending strength of Si nanowires. *Nano Lett.* **2012,** *12*, 2599-2604.

[16] Zhang, H. T.; Tersoff, J.; Xu, S.; Chen, H. X.; Zhang, Q. B.; Zhang, K. L.; Yang, Y.; Lee, C. S.; Tu, K. N.; Li, J. et al. Approaching the ideal elastic strain limit in silicon nanowires. *Sci. Adv.* **2016,** *2*, e1501382.

[17] Tang, D. M.; Ren, C. L.; Wang, M. S.; Wei, X. L.; Kawamoto, N.; Liu, C.; Bando, Y.; Mitome, M.; Fukata, N.; Golberg, D. Mechanical properties of Si nanowires as revealed by in situ transmission electron microscopy and molecular dynamics simulations. *Nano lett.* **2012,** *12*, 1898-1904.

[18] Banerjee, A.; Bernoulli, D.; Zhang, H. T.; Yuen, M. F.; Liu, J. B.; Dong, J. C.; Ding, F.; Lu, J.; Dao, M.; Zhang, W. J. et al. Ultralarge elastic deformation of nanoscale diamond. *Science* **2018,** *360*, 300.

[19] Nie, A. M.; Bu, Y. Q.; Li, P. H.; Zhang, Y. Z.; Jin, T. Y.; Liu, J. B.; Su, Z.; Wang, Y. B.; He, J. L.; Liu, Z. Y. et al. Approaching diamond's theoretical elasticity and strength limits. *Nat. Commun.* **2019,** *10*, 5533.

[20] Ju, S. H.; Facchetti, A.; Xuan, Y.; Liu, J.; Ishikawa, F.; Ye, P. D.; Zhou, C. W; Marks, T. J.; Janes, D. B. Fabrication of fully transparent nanowire transistors for transparent and flexible electronics. *Nat. Nanotechnol.* **2007,** *2*, 378-384.

[21] Cui, Y.; Zhong, Z. H.; Wang, D. L.; Wang, W. U.; Lieber, C. M. High performance silicon nanowire field effect transistors. *Nano Lett.* **2003,** *3*, 149-152.

[22] Kim, D. H.; Ahn, J. H.; Choi, W. M.; Kim, H. S.; Kim, T. H.; Song, J. Z.; Huang, Y. Y.; Liu, Z. J.; Lu, C.; Rogers, J. A. Stretchable and foldable silicon integrated circuits. *Science* **2008,** *320*, 507-511.

[23] Troughton, J.; Bryant, D.; Wojciechowski, K.; Carnie, M. J.; Snaith, H.; Worsley, D. A.; Watson, T. M. Highly efficient, flexible, indium-free perovskite solar cells employing metallic substrates. *J. Mater. Chem. A* **2015,** *3*, 9141-9145.

[24] Nejand, B. A.; Nazari, P.; Gharibzadeh, S.; Ahmadi, V.; Moshaii, A. All-inorganic large-area low-cost and durable flexible perovskite solar cells using copper foil as a substrate. *Chem. Commun.* **2017,** *53*, 747-750.

[25] Jing, H.; Peng, R.; Ma, R. M.; He, J.; Zhou, Y.; Yang, Z.; Li, C. Y.; Liu, Y.; Guo, X.; Zhu, Y. et al. Flexible ultrathin single-crystalline perovskite photodetector. *Nano Lett.* **2020**.

[26] Liu, X.; Guo, X. Y.; Lv, Y.; Hu, Y. S.; Lin, J.; Fan, Y.; Zhang, N.; Liu, X. Y. Enhanced performance and flexibility of perovskite solar cells based on microstructured multilayer transparent electrodes. *ACS Appl. Mater. Interfaces* **2018,** *10*, 18141-18148.

[27] Ahn, S. M.; Jung, E. D.; Kim, S. H.; Kim, H.; Lee, S.; Song, M. H.; Kim, J.Y. Nanomechanical approach for flexibility of organic-inorganic hybrid perovskite solar cells. *Nano Lett.* **2019,** *19*, 3707-3715.

[28] Tian, B. Z.; Xie, P.; Kempa, T. J.; Bell, D. C.; Lieber, C. M. Single-crystalline kinked semiconductor nanowire

superstructures. *Nat. Nanotechnol.* **2009,** *4*, 824-829.

[29] Naji, K.; Dumont, H.; Saint-Girons, G.; Penuelas, J.; Patriarche, G.; Hocevar, M.; Zwiller, V.; Gendry, M. Growth of vertical and defect free InP nanowires on $SrTiO_3$ (001) substrate and comparison with growth on silicon. *J. Cryst. Growth* **2012,** *343*, 101-104.

[30] Meng, Y.; Lan, C. L.; Li, F. Z.; Yip, S. P.; Wei, R. J.; Kang, X. L.; Bu, X. M.; Dong, R. T.; Zhang, H.; Ho, J. C. Direct vapor-liquid-solid synthesis of all-inorganic perovskite nanowires for high-performance electronics and optoelectronics. *ACS Nano* **2019,** *13*, 6060-6070.

[31] Lei, Y. S.; Chen, Y. M.; Zhang, R. Q.; Li, Y. H.; Yan, Q. Z.; Lee, S. H.; Yu, Y. G.; Tsai, H. H.; Choi, W. J.; Wang, K. P. et al. A fabrication process for flexible single-crystal perovskite devices. *Nature* **2020,** *583*, 790-795.

[32] Li, J.; Shan, Z. W.; Ma, E. Elastic strain engineering for unprecedented materials properties. *MRS Bull.* **2014,** *39*, 108-114.

[33] Zhu, C.; Niu, X. X.; Fu, Y. H.; Li, N. X.; Hu, C.; Chen, Y. H.; He, X.; Na, G. R.; Liu, P. F.; Zai, H. C. et al. Strain engineering in perovskite solar cells and its impacts on carrier dynamics. *Nat. Commun.* **2019,** *10*, 815.

Electronic Supplementary Material

High elasticity of $CsPbBr_3$ perovskite nanowires for flexible electronics

Xiaocui Li[1,§], You Meng[2,§], Rong Fan[1,3,§], Sufeng Fan[1], Chaoqun Dang[1], Xiaobin Feng[1], Johnny C. Ho[2] (✉), Yang Lu[1,4] (✉)

[1] *Department of Mechanical Engineering, City University of Hong Kong, Hong Kong SAR 999077, China*
[2] *Department of Materials Science and Engineering, City University of Hong Kong, Hong Kong SAR 999077, China*
[3] *School of Automotive Engineering, Dalian University of Technology, Dalian 116024, China*
[4] *Nano-Manufacturing Laboratory (NML), Shenzhen Research Institute of City University of Hong Kong, Shenzhen 518057, China*
[§] *These authors contribute equally*

Supporting information to DOI 10.1007/s12274-****-****-* (automatically inserted by the publisher)

Contents

Address correspondence to Johnny C. Ho, johnnyho@cityu.edu.hk; Yang Lu, yanglu@cityu.edu.hk

S1 XRD of $CsPbBr_3$ NWs

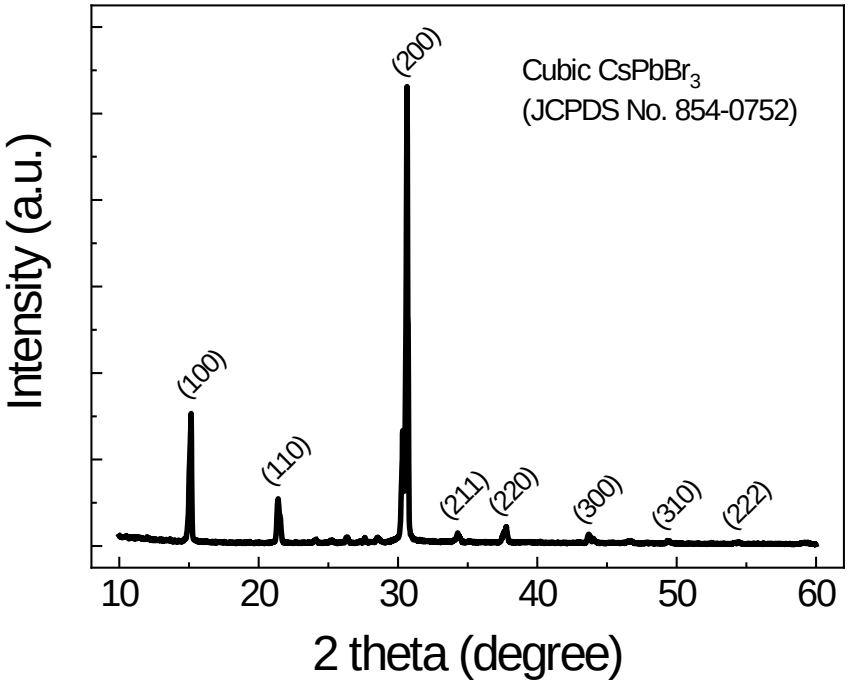

Figure S1 XRD pattern of $CsPbBr_3$ NWs

S2 Plastic deformation and fracture of $CsPbBr_3$ NW

Three more loading-unloading cycles with larger displacement amplitudes were conducted with the NW in Figure 2, as shown in the Figure S2 below and Supplementary Movie 2. In the second cycle (Figs. S2(a)), when fully unloaded, the NW cannot recover to its original straight shape, with local plastic deformation shown, at where the highest strain of this cycle was obtained, as indicated by the red circle. Separated by this 8° kink, the two segments of NW keep well in a straight shape. In the third loading-unloading cycle (Figs. S2(b)), the local plastic deformation was accumulated further at the same point. Finally, the NW was fractured at the fourth loading cycle (Fig. S2(c)). Figs. S2(d)-(f) were FEM simulations of the strain distribution that reproducing the NW geometry prior to unloading or fracture at each cycle, suggesting the highest local tensile strain of ~4.9 %, ~5.4% and ~5.2 % for these three loading-unloading cycles, respectively.

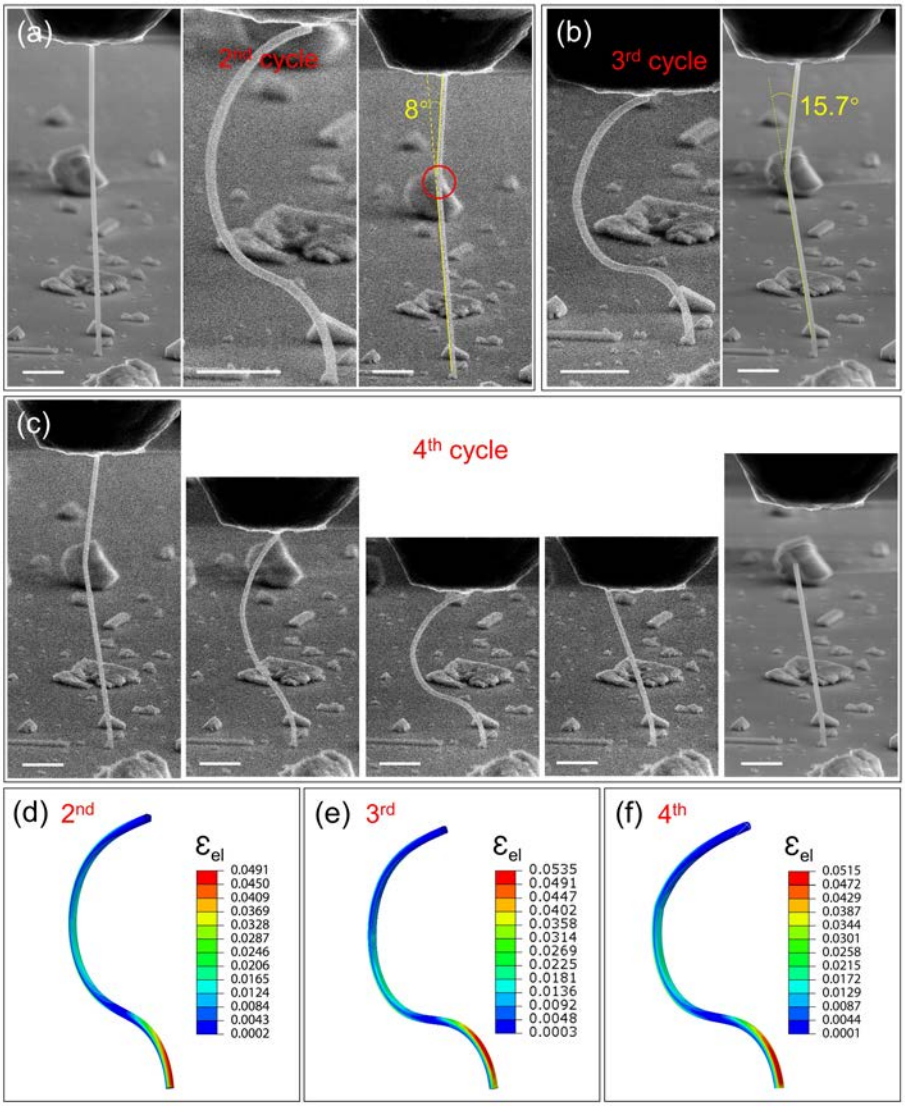

Figure S2 Accumulated local plastic deformation and fracture of $CsPbBr_3$ NW. (a) The second loading-unloading cycle, from this cycle local plastic deformation occurred; (b) The third loading-unloading cycle, with local plastic strain accumulated at the same point of the previous cycle; (c) The fourth loading-unloading cycle, during which the NW finally fractured at the plastically deformed point; (d-f) FEM simulations reproducing the NW geometries prior to unloading/fracture at each cycle. Scale bar in all figures: 2 μm.

S3 Performance characterization of as-fabricated $CsPbBr_3$ NW-based PD.

The current-voltage *(I-V)* curves of PD under light illumination (wavelength: 450 nm, incident power density: 1 mW/cm^2) were measured and shown in Fig. S3(a), with the output current reaching up to ~9 nA. Meanwhile, the PD exhibits excellent reliability in its on/off switching characteristics under light illumination (1 mW/cm^2, 5V) with a chopping frequency of 0.2 Hz. When irradiated, the photocurrent gets increased by ~ 3 orders of magnitude and maintains its high stable value during the entire testing duration (Figs. S3(b) and (c)). Responsivity (R) is another important figure-of-merit to quantify the device performance of PDs, which is defined as $R= I_{light}/(PA)$, where I_{light}, P and A are the light current, incident power density, and effective irradiated area, respectively. The flexible $CsPbBr_3$ NW photodetector shows a R value of 566 A/W, which is comparable to those of recently reported low-dimensional perovskite photodetectors.

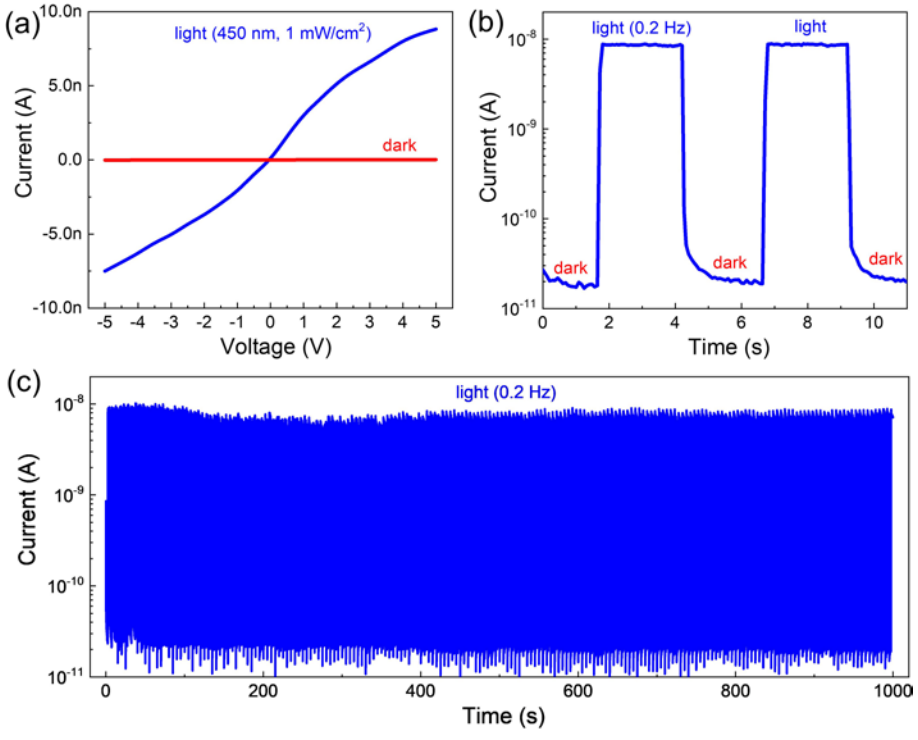

Figure S3 Performance characterization of as-fabricated $CsPbBr_3$ NW-based PD. (a) The current-voltage *(I-V)* curve of the PD under light illumination (1 mW/cm^2). (b, e) Output current of the PD under on/off light illumination (0.2 Hz, 1 mW/cm^2, 5V) as a function of time.

S4 PD performance after 1000, 2000 and 3000 bending cycles

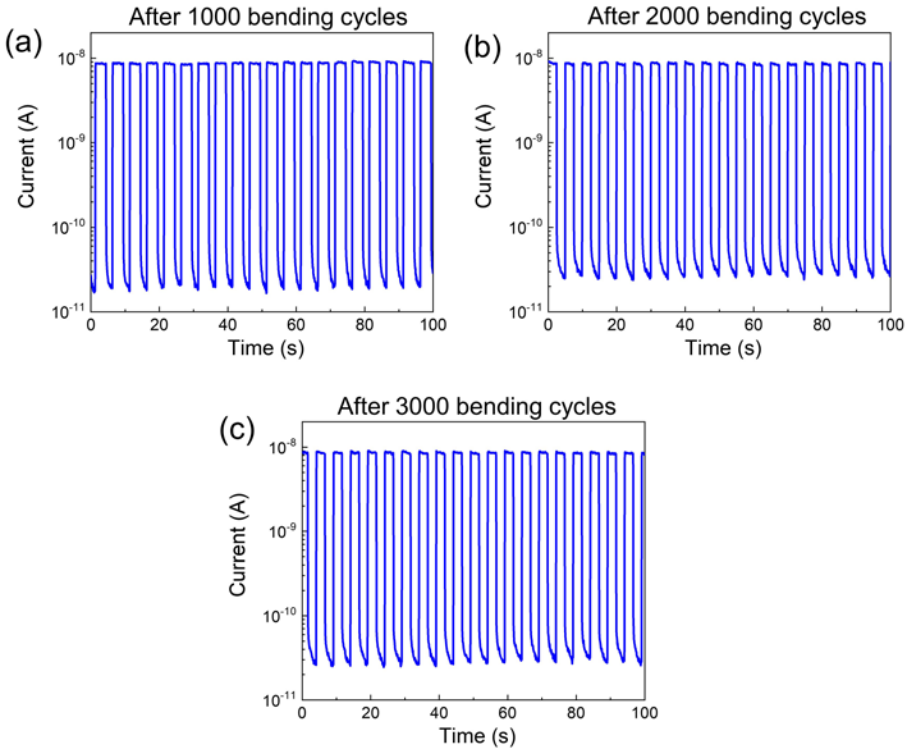

Figure S4 Output current of the PD under on/off switching light illumination after: (a) 1000; (b) 2000; (c) 3000 bending cycles, respectively.

S5 Environmental stability of PD

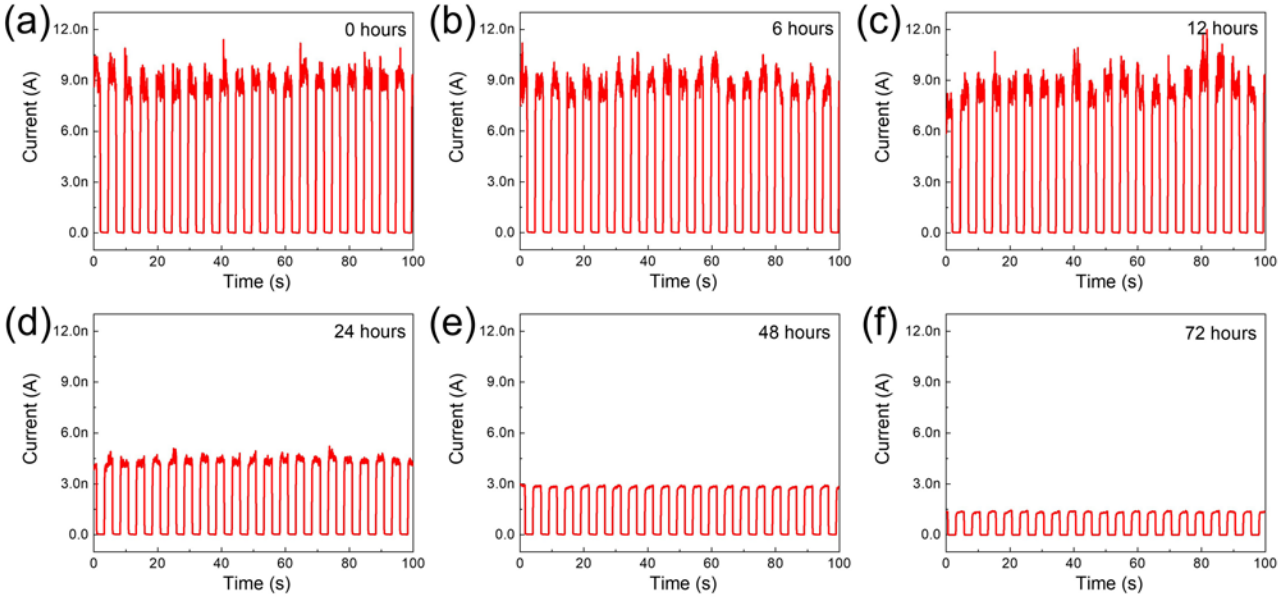

Figure S5 Environmental stability of PD. (a-f) Show the device output current under the 0.2-Hz chopped light illumination (1 mW/cm^2) with a source-drain voltage of 5 V.